JOURNAL OF GEOPHYSICAL RESEARCH, VOL. 105, NO. E5, PAGES 12,023–12,033, MAY 25, 2000

# Lunar polar topography derived from Clementine stereoimages

A. C. Cook,[1] T. R. Watters,[1] M. S. Robinson,[2] P. D. Spudis,[3] and D. B. J. Bussey[4]

**Abstract.** Clementine stereoimagery has been used to produce digital elevation models of the Moon, at a scale of ~1 km/pixel. These models cover regions poleward of 60° in both hemispheres and reveal topography beyond that covered by the Clementine laser altimeter or Earth-based radar. By combining these polar terrain models with the current Clementine laser altimeter data we have produced a global topographic map of the lunar surface. Several topographic features in the new polar topographic data set are described, including three previously unrecognized pre-Nectarian impact basins. Several known basins have also been mapped, including the southern extent of the South Pole-Aitken basin, and other previously suspected basins have been verified.

## 1. Introduction

The Clementine spacecraft was launched on January 25, 1994, and was placed into a 5 hour (400 × 2940 km) lunar polar mapping orbit on February 19, 1994 [*Nozette et al.*, 1994]. Approximately 600,000 ultraviolet-visible (UV-VIS) camera images were taken of the lunar surface, mostly in the nadir-pointing direction. Complete global coverage was obtained, including regions that were poorly known from earlier Lunar Orbiter satellites due to low-resolution and restricted illumination conditions.

Previous efforts at studying the topography of the poles have included photographic limb profiles [*Watts*, 1963], heliometric measurements [*Nefediev*, 1958], and Earth-based stellar grazing occultation profiles [*Appleby and Morrison*, 1983]. However, these methods reveal only angular deviations from the Moon's mean limb as seen from Earth, along the line of sight. The Clementine spacecraft carried a laser altimeter which returned ~72,000 usable height measurements of the surface which in turn were used to define the lunar geoid [*Zuber et al.*, 1994; *Smith et al.*, 1997]. Although this instrument produced highly detailed topographic profiles along north-south tracks, large gaps between profiles of ~60 km exist due to the 2.5° mean orbit spacing in the cross-track direction at the equator. No laser returns were obtained within 11° and 8° of the south and north poles, respectively, because of the maximum altitude limits under which the laser altimeter could operate. The laser altimeter spot size was ~200 m at periselene, and the spacing between measurements was ~20 km along track [*Smith et al.*, 1997]. Thus the height measurements returned become increasingly less representative of the surrounding terrain as the spacecraft moved from relatively flat mare areas into the rugged highlands.

Recent results, with a height and spatial resolution of ~50 and ~150 m, respectively, have been obtained by using Earth-based radar interferometry [*Margot et al.*, 1999] applied to the polar regions. Although this technique has the potential to map the topography of the whole lunar near side at this resolution, radar can reach neither the far side of the lunar polar regions beyond the ±7° limits of libration in the latitudinal direction [*Heiken et al.*, 1991] nor the near-side limb areas obscured by local topography.

Another method of obtaining topographic information is the analysis of stereoimages. This technique could not be applied reliably to regional areas using the earlier Lunar Orbiter photographic coverage because of inherent image distortion in the reconstructed images received on Earth. However, topographic photomaps were created for a few localized areas using Lunar Orbiter III and V photographs with 200 and 400 m contour intervals, respectively [*Greeley and Batson*, 1990]. The Apollo missions carried metric and panoramic stereo cameras which were used to produce topographic maps with 100 (50 m supplemental) and 20 m (10 m supplemental) contours, but these were confined to the equatorial zone of the Apollo overflight. Stereoimagery, from the Clementine polar orbiter, found in the overlap region between the mostly nadir-pointing UV-VIS images on any given orbit, can be used to produce digital elevation models (DEMs) of areas beyond the Apollo coverage, including the lunar polar regions [*Cook et al.*, 1996a; *Hoffmann et al.*, 1996; *Spudis et al.*, 1998; *Cook and Robinson*, 1998]. Although the typical stereoangle between adjacent nadir-pointing UV-VIS images is weak (3°–5°), by making use of automated digital stereoanalysis software, a digital terrain model (DTM) (or a collection of longitude/latitude/height points in a tabular ASCII format) tile can be produced for each stereo pair. The DTM tiles can then be fitted to Clementine laser altimeter points, and to each other, to derive a large area DEM or a gridded array of heights in a binary image format) in a polar stereographic map projection. Because of camera position and pointing uncertainties it is estimated that the spatial precision of the final DEM would be not better than ~1 km. Therefore the DEM pixel size was selected to be 1 km. Although stereoheight accuracy predictions [*Cook et al.*, 1996b] suggest it is possible to detect topographic features with a height resolution of 50 m, this refers to stereopairs where the camera was tilted off nadir [*Sorensen*, 1995; *McEwen and Robinson*, 1997]. The matching of such stereopairs is difficult to automate. Our technique utilizes the weaker nadir stereoangle images; however, by combining several stereo matched height measurements together inside each of the 1 km pixels of the

[1]Center for Earth and Planetary Studies, National Air and Space Museum, Washington, D. C.
[2]Department of Geological Sciences, Northwestern University, Evanston, Illinois.
[3]Lunar and Planetary Institute, Houston, Texas.
[4]Space Science Department, European Space Agency/ESTEC, Nordwijk, Netherlands.



Paper number 1999JE001083.
0148-0227/00/1999JE001083$09.00

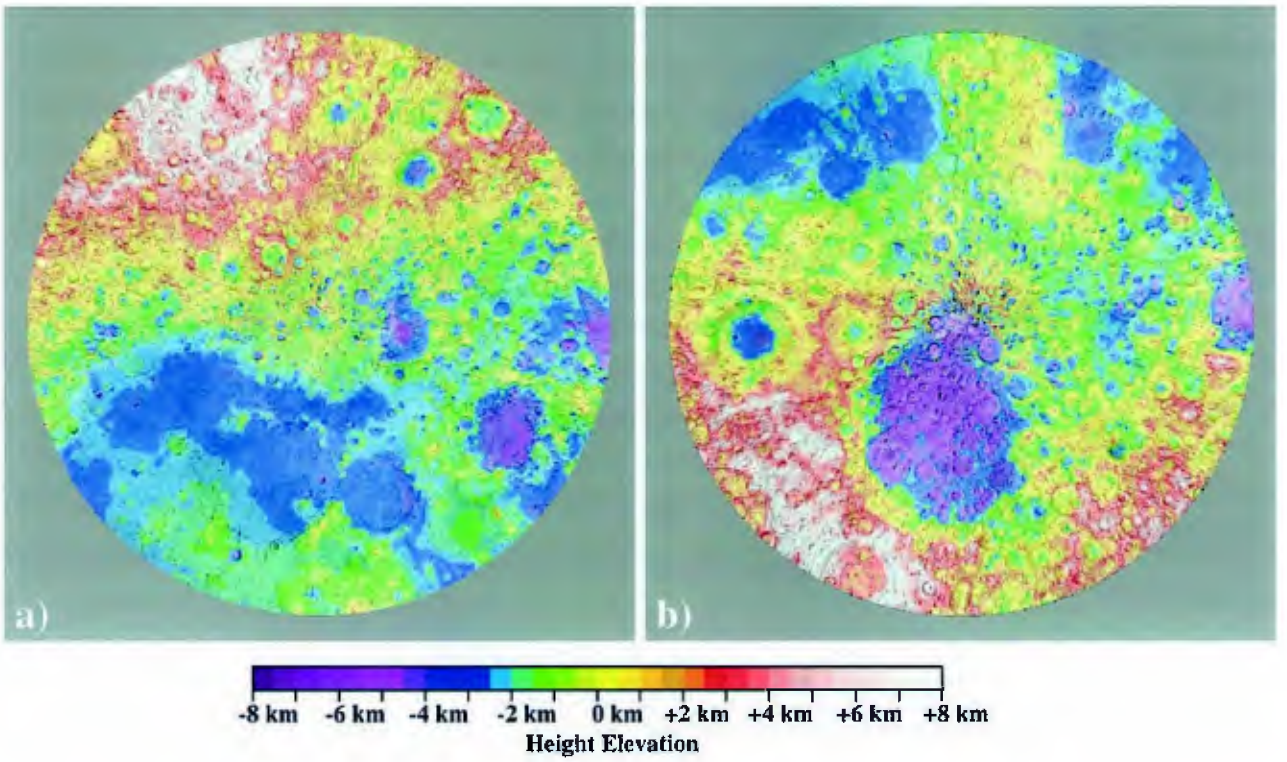


**Plate 1.** Composite of our lunar polar stereo DEMs and a laser altimeter DEM [*Smith et al.*, 1997], color coded for elevation and overlain on a USGS shaded relief map. (a) The entire Northern Hemisphere (0°N to 90°N) and (b) the entire Southern Hemisphere (90°S to 0°N).

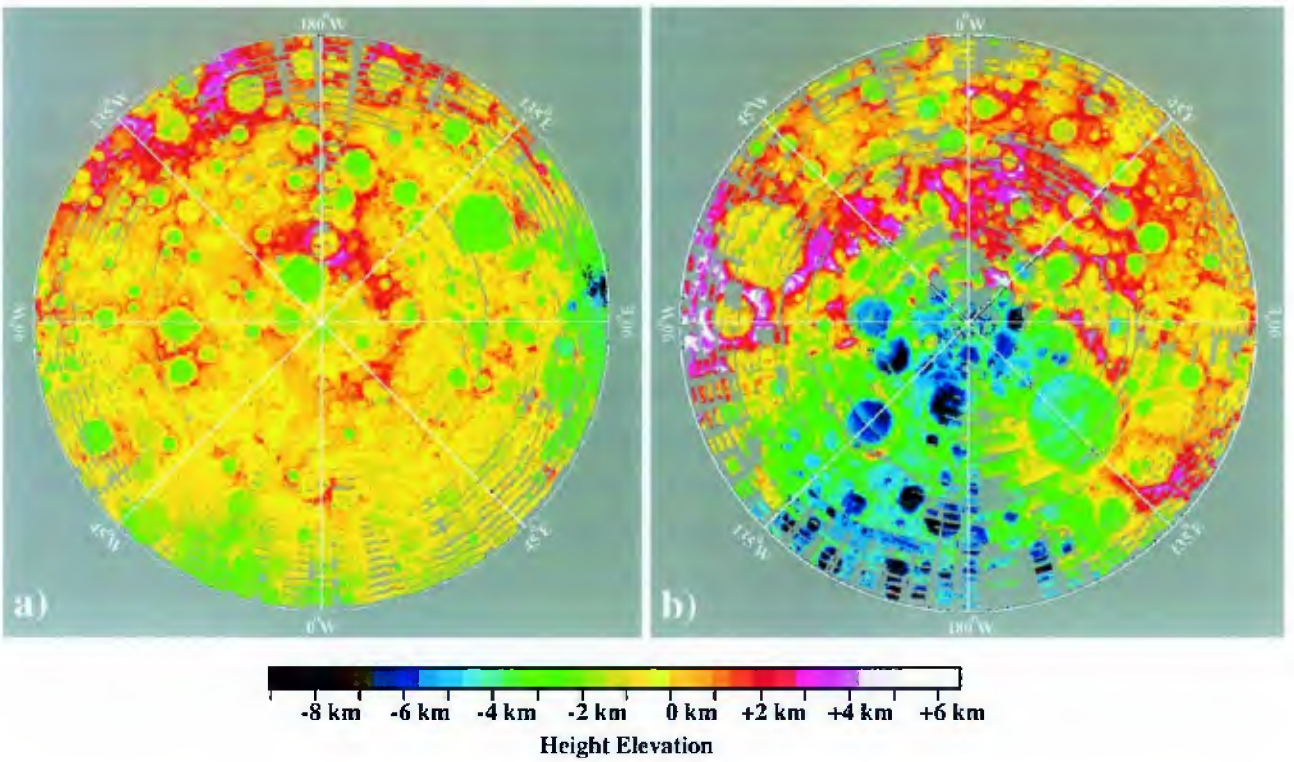


**Plate 2.** Color-coded DEMs of the lunar poles in a polar stereographic projection: (a) the north pole (90°N to 60°N) and (b) the south pole (60°S to 90°S).

final DEM, it is possible to resolve 100 m relative height differences within a DTM tile area. Absolute height errors were derived by computing the standard deviation between Clementine laser altimeter points and the DEMs and found to be ±0.7 km for the south pole DEM and ±0.4 km for the north pole DEM. In the polar regions, outside the laser altimeter measurement zone, absolute height errors cannot easily be determined. However, by varying the choice of the laser altimeter anchor points (see below) close to the polar regions, we have found variations of up to 1 km in absolute elevation.

The UV-VIS images are small, 384 × 288 pixels corresponding to a field of view (FOV) at the poles of ~71 × 53 km at closest approach. The UV-VIS spatial image resolution (effective size of each pixel projected onto the lunar surface) varied from 185 to ~500 m/pixel over the polar regions. Almost 4000 DTM tiles were required to cover the Moon's south pole area (90°S–60°S) and over 5000 DEM tiles to cover the Moon's north pole area (60°N–90°N). On any given south-north orbital pass, the UV-VIS camera undertook a repeating multifilter and dual exposure imaging sequence. In each cycle, typically 10 images were taken in quick succession with two exposures for each of the five filter positions and then this cycle would be repeated after the image field of view had shifted approximately two thirds of a frame width [*McEwen and Robinson*, 1997]. Images obtained during a filter cycle differ in image center position by only a few pixels. Ten DTMs can be produced, utilizing images from adjacent image cycles and then combined into a DTM tile with improved topographic signal to noise ratio. Therefore the number of stereopairs that required processing was 10 times the number of DTM tiles or ~90,000 in total. Because of the imaging sequences, some gaps in stereocoverage result and show up as empty rectangular spaces in the DEMs. It is possible to combine the lunar polar DEMs with existing laser altimeter data [*Smith et al.*, 1997] to produce a map of global topographic coverage of the lunar surface (Plate 1). Plates 2a and 2b show the respective color-coded stereo-derived elevations at the lunar poles. A lunar topographic datum of a sphere with a radius of 1737.4 km was used for all height measurements.

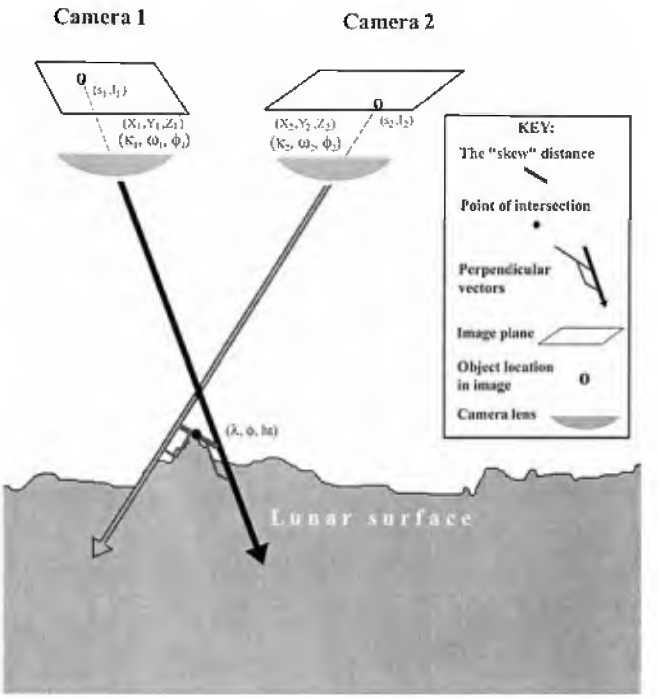


**Figure 1.** Diagram illustrating stereointersection camera modeling. By ray tracing from the sample and line $(s_1,l_1)$ and $(s_2,l_2)$ image coordinates of a common point, using known camera positions $((X_1, Y_1, Z_1)$ and $(X_2, Y_2, Z_2))$ and camera orientation angles $((\kappa_1, \omega_1, \phi_1)$ and $(\kappa_2, \omega_2, \phi_2))$, it is possible to establish the closest point of intersection at the planetary surface. Due largely to small uncertainties in camera navigation parameters, the rays never intersect exactly but are separated by a small "skew" distance. The skew distance varies across the region of stereooverlap within certain limits, and its standard deviation can be used to evaluate the quality of the DTM tiles.

## 2. Method

Generating the Clementine DEMs involved three stages of processing: (1) stereomatching image pairs for each orbit using a patch-based matcher program "Gotcha" [*Day et al.*, 1992], (2) producing DTM tiles, and (3) fitting all the DTM tiles iteratively to produce a combined DEM. For the first stage an automatic algorithm is used to identify some common tie points in each stereopair; these form seed points for the stereomatcher. Each image pair is then stereomatched using a grid spacing (sampling interval) of every three pixels in the image sample and line directions, and a correlation patch radius of seven pixels. In the second stage of processing, the common matched points for each stereopair are fed through a stereointersection camera model (Figure 1) to produce a DTM. JPL NAIF software and kernels are used to compute spacecraft position and camera orientation utilized by the stereointersection camera model. These data overlay images on the lunar surface to better than 1 km relative to each other cross track, hence the pixel size for the final DEM was chosen to be 1 km. The 1 km relative uncertainty in image geocoding to the surface also results in an absolute height offset error of each DTM tile, but this is removed by a tile-fitting process described below. For some DTMs the stereomatching process may go wrong because of a lack of scene contrast or noise. Therefore individual DTMs making up a DTM tile are rejected if (1) they contain fewer than 100 points, (2) their mean elevation exceeds ±25 km, (3) their mean stereointersection skew separation distance (Figure 1) exceeds 2 km, or (4) their height standard deviation exceeds 5 km. For the formation of a DTM tile, a reference DTM must be found for which other DTMs can be zero-offset against. The DTM with the smallest standard deviation on its stereointersection skew value (the pair with the highest quality of matching) is selected as a reference DTM. Two methods are used to reduce the effects of noise present within the DTMs: (1) median filtering within pixels, (2) the relative height offset is determined using the mode of the height differences between each DTM and the reference. Finally, after correcting each DTM for height offsets, the results are combined into a "DTM tile."

The third stage involves generating a reference DEM, initially containing all laser altimeter points. DTM tiles can then be fitted to this reference DEM if underlying laser altimeter points are present. The reference DEM is updated with the fitted tiles and the process repeated iteratively. When the iterations are complete, or when no further overlapping tiles could be fitted to altimeter points or to previously fitted DTM tiles, laser altimeter points are tested to see which deviate the most. Laser altimeter points, which show a large offset, thus

**Table 1.** Total Number of All Clementine Laser Altimeter Points Contained Within Latitude Limits for Polar Regions

| Latitude Range | Number of Altimeter Points | Latitude Range | Number of Altimeter Points |
|---|---|---|---|
| 90°N–84°N | 0 | 90°S–84°S | 0 |
| 84°N–82°N | 2 | 84°S–82°S | 0 |
| 82°N–80°N | 7 | 82°S–80°S | 0 |
| 80°N–78°N | 47 | 80°S–78°S | 11 |
| 78°N–76°N | 107 | 78°S–76°S | 86 |
| 76°N–74°N | 154 | 76°S–74°S | 171 |
| 74°N–72°N | 221 | 74°S–72°S | 213 |
| 72°N–70°N | 374 | 72°S–70°S | 269 |

indicating that they are unreliable, are removed from the reference DEM and the entire process repeats. Any DTM tiles that cannot be fitted to underlying laser altimeter points, or to adjacent tiles, are fitted to interpolated laser altimeter points instead, though due to extensive DTM tile overlap this was quite rare. Finally, the updated DEM is saved as a polar stereographic floating point image.

Note that laser altimeter point measurements do not exist for the region below 79°S or above 83°N (Table 1) and their reliability decreases toward the poles, especially in highland terrain [*Smith et al.*, 1997]. In order to cover these two areas the DTM tile-fitting process anchors initially to the highest-latitude absolute height points (Clementine laser altimeter points and any existing fitted DTM tiles) and then gradually steps poleward. This process fits iteratively to previously anchored tiles until complete coverage (circular closure) is obtained at the poles. Because the DTM tiles poleward of the highest-latitude altimeter points overlap each other in latitude rings, and these cover all longitudes, relative DTM height errors should average out. However, it has been found that by changing the selection of altimeter points, or the DEM pixel size, the absolute elevation in the nonlaser altimeter-controlled polar regions can change by as much as 1 km. The errors on the relative elevations within a DTM tile on the DEM allow resolution of topography of ~100 m, although between DTM tiles, height offsets can sometimes be ~300 m absolute. These limitations have minimal impact on the results described in this paper, which deal mostly with relative elevations.

## 3. The Lunar North Pole

### 3.1. Sylvester-Nansen Basin

The new stereo-derived DEM has allowed the recognition of a basin previously not identified in conventional orbital images. The impact basin, centered at 45°E, 83°N (Table 2, Plates 1a and 2a and Figure 2) and which we refer to as the Sylvester-Nansen basin [*Cook et al.*, 1999a], is shallow (Figure 3), and its rim and interior are extensively degraded by overlying younger craters and deposits which makes identification in images difficult. The Sylvester-Nansen basin has a topographic ring of 300–500 km in diameter and a ring elevation above the exterior terrain of 1–2 km (Plate 2 and Figure 2). However, because the basin is almost centered on the north pole, and DTM tiles have a concentric pattern, it was necessary to check that the topographic features that mark the basin were not due to some processing artifact. The DEM generation process was repeated with 2 km pixels (to reduce topographic noise and to increase the chances of DTM tile overlap) for trial runs using images from separate phases of the mission: the premapping phase, first, second, and third months [*Nozette et al.*, 1994; *McEwen and Robinson*, 1997]. The DEMs from the premapping and first-month mapping orbits both contain large-area overlapping DTM tiles and reveal a basin depression, although topographic noise is noticeable. The DEMs generated from the second and final month images are made from more numerous smaller DTM tiles, contain less topographic noise, but show little evidence for a basin depression. However, in all versions of DEMs generated, we always see a topographic ring and so conclude that at least the basin ring exists. Evidence for the basin ring structure on the near side of the Moon can be seen in a delay Doppler radar image [*Stacy et al.*, 1997] and perhaps also on the far side in a Clementine UV-VIS mosaic (Figure 4). Although not conclusive proof for a basin by itself, a negative gravity anomaly can also be seen at the location of the basin center in the Lunar Prospector gravity map [*Konopliv et al.*, 1998; *Konopliv and Yuan*, 1999]. The geologic map of *Lucchitta* [1978] shows that the basin interior contains numerous craters with floor fills of Imbrium undivided plains material and various terra units filling the intercrater plains. The geologic map also reveals that several of these craters (e.g., Peary, Byrd, Hermite, Rozhdestvensky, and Nansen) have highly subdued rims (pNc material); therefore we interpret the basin to be pre-Nectarian in age.

The northern half of the floor of the Nansen (95°E, 81°N) crater (Plate 2a and Figures 2 and 5) is covered with a 1.3 km thick deposit which is interpreted [*Lucchitta*, 1978] as being Nectarian age (Nbl) lineated basin material, presumably from the Humboldtianum basin (centered on 83°E, 57°N, and ~500 km in diameter). The boundary of this material appears to lie on a lineament running 300 km from just northeast of the Sitter crater (40°E, 80°N) to the east edge of Nansen crater. The rim of Peary crater (33°E, 89°N) bisects the North Pole at an absolute height of ~ −0.7 km. The crater Plaskett (174°E, 82°N) has the highest elevation (+4.1 km) within 800 km of the lunar north pole.

### 3.2. Schwarzchild Basin

The Schwarzchild basin (Plate 2a and Figures 2, 6, and 7) is a 220 km diameter transitional basin (centered on 121°E,

**Table 2.** Newly Discovered and Confirmed Basins

| Basin | Status | Center | Diameter 1 | Diameter 2 |
|---|---|---|---|---|
| Amundsen-Ganswindt | confirmed | (120°E, 81°S) 122°E, 81°S | (355 km) 360 km | |
| Bailly-Newton | new | 57°W, 73°S | 330 km | |
| Dirichlet-Jackson [*Cook et al.*, 1999b] | confirmed | 158°W, 14°N | 470 km | |
| Schrödinger-Zeeman | new | 165°W, 81°S | 150 km | 250 km |
| Sikorsky-Rittenhouse | confirmed | (68.5°S, 111°E) 110°E, 68°S | (310 km) 270 km | |
| Sylvester-Nansen | new | 45°E, 83°N | 300–500 km | |

Values in parentheses indicate previously accepted diameter values [*Wilhelms*, 1987].

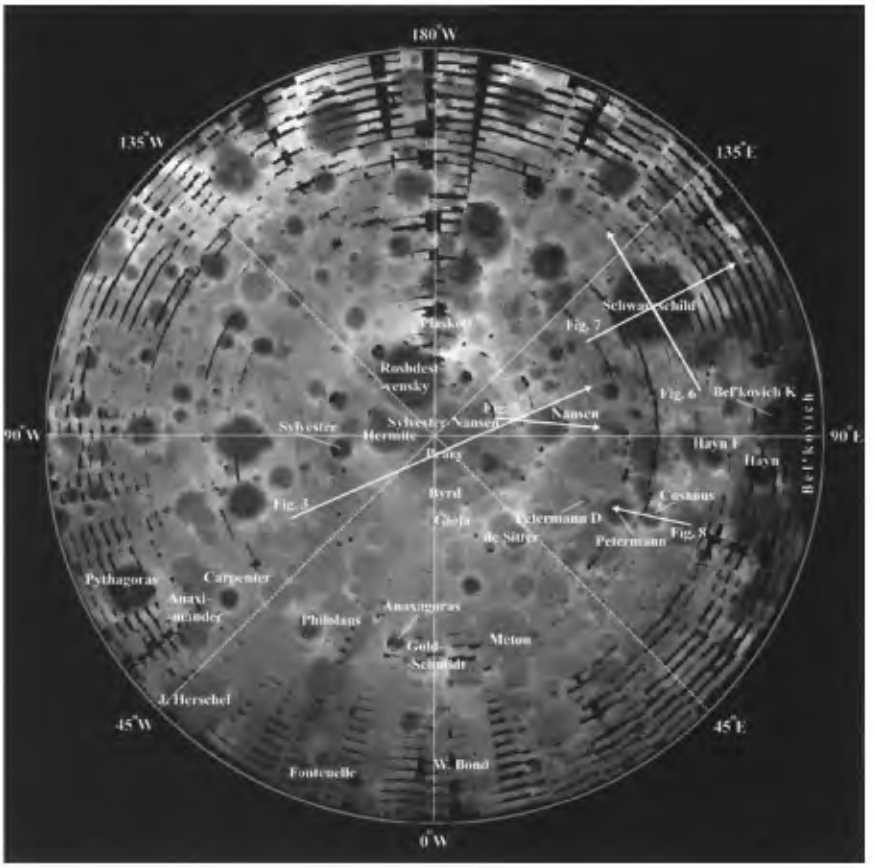


**Figure 2.** Locations of topographic profiles (see corresponding figure numbers) and selected named features in the north polar area overlain on a grey-scale DEM (black <= −4.1 km, white >= +3.7 km, and no data is also designated black).

70°N) [*Lucchitta*, 1978] and has a relatively flat uniform floor −3.2 km below the lunar datum) with a mean rim height 3.1 km above the floor and a maximum absolute height elevation of +2.3 km on a portion of the southwest rim. The central ring of hills stand, on average, 0.7 km above the floor a maximum elevation of 1.3 km. An interior 44 km diameter crater attains a depth of 0.9 km beneath the floor. The topography of the basin ejecta extends some 50 km beyond the outer ring.

A 170 km diameter buried crater may lie to the east of the Schwarzchild basin beneath NpNt Nectarian and pre-Nectarian terra material and is therefore older. The southwest edge of the Schwarzchild basin is depressed where it intersects with the outer ring of the Bel'kovich basin, and three buried craters (140, 90, and 70 km diameter) are visible. They have been depicted on a geologic map [*Lucchitta*, 1978] as buried by lineated basin material; however, the DEM shows the map to be slightly in error with regard to their position and extent.

### 3.3. Bel'kovich Basin

Utilizing Galileo stereo images, *Oberst et al.* [1996] revealed the topography of the Humboldtianum basin and the interior of the Bel'kovich basin for the first time. Our DEM (Plate 2a and Figure 2) improves the spatial resolution above 60°N, over the Galileo stereo-derived DEM, and shows the northern extent of both basins. The deepest point in the basin system above 60°N is at 5.7 km below the lunar datum on the floor of the Bel'kovich *K* crater. In general, a little sign of a proposed Bel'kovich basin outer ring structure [*Lucchitta*, 1978] can be seen in the DEM; however, topographic anomalies are visible along the path of the proposed ring at craters: Hayn, Hayn F, and Cusanus. The southwest rim of the Copernican-age 90 km diameter Hayn crater (83°E, 65°N) has a rim peak which attains an elevation of 6 km above its floor and a graben running north-south across the floor of the crater which bisects the 1

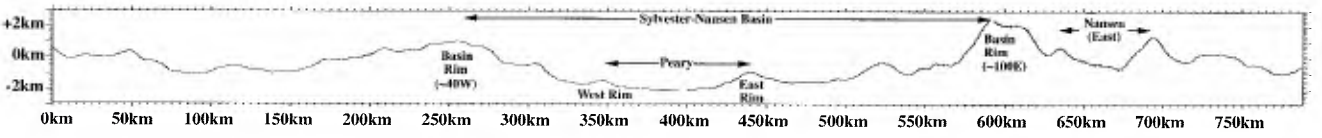


**Figure 3.** Topographic profile through the Sylvester-Nansen basin (60°W, 77°N to 108°E, 77°N) with 10X vertical exaggeration. Note that the apparent basin depression may be an artifact of the processing and is perhaps not so deep; however, the subdued basin rim appears to be genuine.

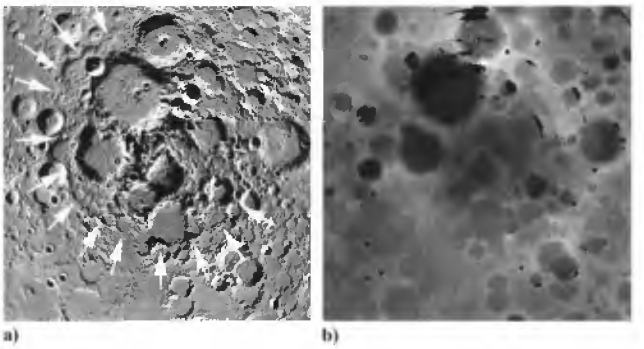


**Figure 4.** (a) Clementine UV-VIS mosaic of the lunar north pole. Arrows indicate evidence for the Sylvester-Nansen basin ring on the near side. Arrows with question marks indicate possible evidence for the basin ring on the far side. (b) Corresponding region of the grey-scale DEM (black = −3.7 km, white = +4.3 km, and black also indicates no data).

km high central peaks. The Hayn *F* crater is a 66 km diameter Nectarian crater, just to the north of Hayn, and has a high peak on its SSW rim standing some 5.6 km above its floor. A crater chain, nonradial to the basin, is visible in the DEM to the east of the Petermann *D* crater and down the eastern side of Petermann (66°E, 74°N) and Cusanus (71°E, 72°N) craters, the latter of which has a ~600 m deep interior moat (Figure 8).

### 3.4. Imbrium Basin, Northern Exposure

The DEM reveals a distinct break in slope between the craters J. Herschel and W. Bond corresponding to the mapped contact [*Lucchitta*, 1978] between Mare Frigoris and the Fra Mauro formation to the north. The outer ring of the Imbrium basin may be visible in the DEM (Plates 1a, 2a, and Figure 2) where a topographic front has been created by the craters Philolaus and Goldschmidt. Several examples of lineated grooves are present on the northern limits of Mare Frigoris and are a result of secondary impacts from the Imbrium event.

The track of a 400 km long secondary crater chain or ejecta scour mark (Figure 9) can be seen starting near Fontenelle D crater (23.4°W, 62.5°N) and passing northwest of Fontenelle crater (19°W, 63.5°N), where it is 50 km wide. The scour mark then passes through the eastern half of the Philolaus B crater (22°W, 72°N), where it forms a 45 km wide flat-floored trough (1.1 km deep) at 73°N (along the 20°W longitude line between the Philolaus and Anaxagoras craters). The track terminates in the DEM at 78°N. The close alignment of a couple of short parallel scour marks with ridges, just southwest of Gioja crater (14°W, 80°N), may suggest a continuation of the 400 km track out to a total distance of 550 km from Fontenelle D. Other prominent but shorter scour marks can be seen on either side of the crater W. Bond (4°W, 65°N). The southern rims of the Goldschmidt (4°W, 73°N), Barrow (8°E, 71°N), and Meton (19°E, 74°N) craters are breached in several places by lineated

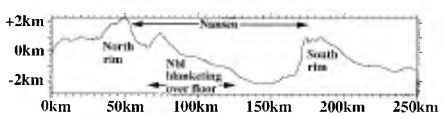


**Figure 5.** Topographic profile through Nansen crater (107°E, 85°N to 93°E, 77°N) with a vertical exaggeration of 10X.

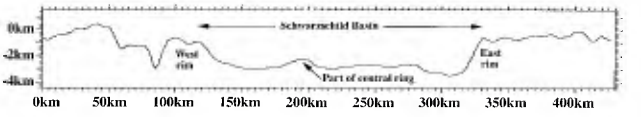


**Figure 6.** Topographic (W-E) profile through the Schwarzschild basin (100°E, 69°N to 140°E, 69°N) with a vertical exaggeration of 10X.

troughs which are associated with the ejecta sculpture of the Imbrium basin [*Lucchitta*, 1978]. On the west of the DEM (Figure 2) a valley bisects the north rim of the flat-floored J. Herschel 100 km diameter crater (42°W, 63°N) and runs into the Anaximander craters (51°W, 67°N).

## 4. The Lunar South Pole

### 4.1. Schrödinger Basin

The interior of the Schrödinger basin (diameter 312 km, centered on 132°E, 75°S) is horizontal in the east-west direction with a typical dynamic height range of 1 km (Plate 2b and Figures 10 and 11). In the north to south direction the basin dips 0.2° toward (Figure 12) the south pole, thus making the southern floor ~1 km lower than the northern floor. The interior mountain ring in the Schrödinger basin attains a maximum height of 2.5 km above the floor. Rilles on the floor of the Schrödinger basin [*Shoemaker et al.*, 1994] can be seen in the DEM. Several linear troughs are adjacent and radial to the Schrödinger basin. The most prominent of these is Rima Schrödinger, which is ~400 km long, has a maximum width of ~15 km, and is up to 600 m deep. A linear feature, aligned with Rima Schrödinger, extends across the floor of the Schrödinger basin and cuts through its rim; this linear feature is visible in a NASA-rectified Lunar Orbiter IV image (frame 10M shown in Figure 13). Zeeman crater (134°W, 75°S) also has a linear trough cutting across its rim which may be associated with troughs radial to the Schrödinger basin. The origin of Rima Schrödinger and other linear troughs is not well understood. Sections of Rima Schrödinger and nearby Rima Planck (also radial to the Schrödinger basin) have raised rims and appear to consist of arcuate segments. These raised arcuate segments may be the result of overlapping impact craters. This suggests that the linear troughs were formed by lines of coalescing secondary craters [*Wilhelms et al.*, 1979; *Melosh*, 1989] from the Schrödinger basin or possibly another basin. However, other sections of these troughs exhibit straight walls with no evidence of raised rims. These troughs could be interpreted to be fractures if they were not continuous with trough segments with raised rims. Thus although linear troughs with straight walls are more consistent with a tectonic origin, troughs with raised rims strongly suggest they formed by an impact process. Neither of the two hypotheses can be unequivocally ruled out with the available data.

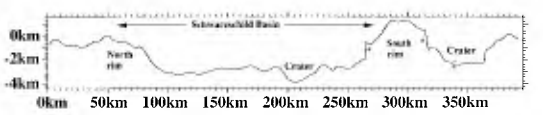


**Figure 7.** Topographic (N-S) profile through the Schwarzschild basin (122°E, 76°N to 120°E, 63°N) with a vertical exaggeration of 10X. The asterisks refer to localized areas where DTM tiles mismatch and false topographic steps result.

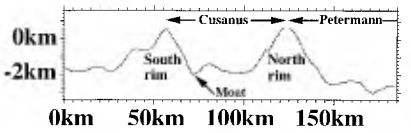


**Figure 8.** Topographic profile through the Casanus crater (71°E, 69°N to 68°E, 75°N) with a vertical exaggeration of 10X.

### 4.2. Sikorsky-Rittenhouse Basin

Sikorsky-Rittenhouse basin (270 km diameter, centered on 110°E, 68°S) was tentatively identified as an ancient buried basin (Plate 2b and Figures 10 and 14) [*Wilhelms*, 1987]. The DEM reveals that Sikorsky-Rittenhouse is a basin in its own right and not part of the South Pole Aitken basin, having a subdued outer ring and possibly a highly degraded ~500 m high inner ring of hills. This inner ring has a diameter of ~100 km and a width of ~20 km. These massifs could alternatively be the remains of a highly degraded crater. The center of this basin is bisected by Rima Schrödinger (up to 600 m deep) and a parallel shallow broader linear trough to the east. The easternmost of these features appears to deflect around the proposed central hill ring. The region between Rima Schrödinger and the parallel linear trough is raised by up to ~500 m and is also clearly visible on the Lunar Orbiter IV frame 10M (Figure 13).

### 4.3. Amundsen-Ganswindt Basin

The new DEM confirms that this previously suspected degraded basin is 360 km diameter (Plate 2b and Figures 10 and 15) and lies (centered on 122°E, 81°S) between the Schrödinger basin and the south pole. The basin predates the Schrödinger basin and is pre-Nectarian in age [*Wilhelms*, 1987]. Any inner ring has been obliterated by overlying craters across its floor, some up to 100 km in diameter. The basin slopes towards the south, like the Schrödinger basin, and its deepest point lies inside the Amundsen crater (86°E, 84°S), 7.7 km below the datum.

### 4.4. Bailly Basin

Bailly is a 300 km diameter basin, centered on 69°W, 67°S (Plate 2b and Figures 10 and 16) and has a multitude of craters covering its floor, the largest being 55 km in diameter. There is no evidence for an interior ring in the topography, presumably because it has been buried by basin deposits and ejecta from Hausen crater to the east [*Wilhelms et al.*, 1979].

### 4.5. Schrödinger-Zeeman

We have discovered an impact basin, which we refer to as the Schrödinger-Zeeman basin [*Cook et al.*, 1999a] (Plate 2b and Figures 10 and 17) which is centered at 165°W, 81°S. This basin is just visible in a UV-VIS Clementine mosaic (Figure 18) and correlates with a gravity anomaly revealed in the Lunar Prospector data [*Konopliv et al.*, 1998; *Konopliv and Yuan*, 1999]. The Schrödinger-Zeeman basin has a double-ring structure with diameters of 150 and 250 km. The interior floor has an absolute elevation of −6.8 km, and the maximum absolute height on the northern part of the inner ring is −2.9 km. The width of the inner ring is 30 km; the outer ring is less intact and varies from 10 to 20 km in width. The area between Schrödinger and Zeeman is overlain by Nectarian-age basin-lineated material [*Wilhelms et al.*, 1979], a basin deposit that has a morphology similar to the younger Hevelius formation (basin ejecta from the Orientale basin). Because of burial by Nectarian-age ejecta, and the fact that this basin appears highly degraded and similar to the two other pre-Nectarian basins described in this paper, we conclude that the Schrödinger-Zeeman basin is pre-Nectarian in age.

### 4.6. South Pole Basin

It has been suggested that there might be a 300 km diameter basin located at the south pole [*Shoemaker et al.*, 1994]. However, we see no evidence to confirm or negate this idea, based on the new topography. The area lies in the depression formed from the South Pole-Aitken basin where there are numerous overlapping craters. The height of the rim of Shackleton crater (0°W, 90°S) is −2.9 km (absolute elevation) and low lying, as is much of the surrounding terrain, apart from a few nearby peaks, hence parts of the rim of the Shackleton crater are illuminated for much of the time [*Bussey et al.*, 1999]. The lowest point in the region lies 7.7 km below the datum (Plate 2b) on the floor of the Amundsen crater. The highest point (41°E, 84.6°S) may lie on a plateau east of Malapert (which is part of the South Pole-Aitken basin rim (see below)) where the elevation is ~5 km above the Moon's mean radius.

### 4.7. South Pole-Aitken Basin (SPA)

Our DEM covers the southern limits of the SPA basin (Plate 1b) which were not mapped by the Clementine laser altimeter [*Spudis et al.*, 1994]. The ring structure of the SPA basin (centered on 180°E, 50°S, diameter 2600 km) can be seen in the DEM (Plate 2b), with a section of the *Wilhelms et al.* [1979] proposed outer ring (Figure 10) clearly revealed in the topography, just south of Bailly basin. The "crater" Malapert (13°E, 85°S) is actually a trough between two massifs trending transverse to the Earth direction. These massifs are part of the Liebnitz Mountains, the near-side expression of the SPA basin rim crest. Another section of ring structure can be seen on the western edge of the Schrödinger and Amundsen-Ganswindt basins. There is a scattering of high terrain in the vicinity of Simpelius crater (15°E, 73°S) which could be associated with the SPA basin, or alternatively the Mutus-Vlacq basin (cen-

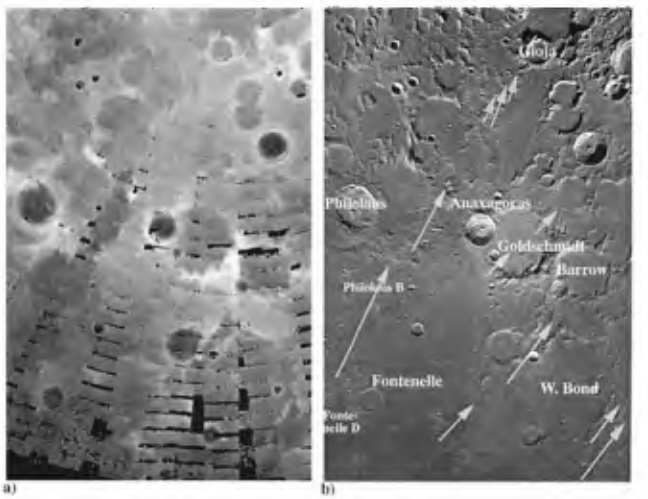


**Figure 9.** Scour marks on the near side of the lunar north pole region in (a) grey-scale DEM (black <= −3.9 km, white >= +1.8 km, and black also indicates no data) and (b) a Clementine mosaic with crater labels and arrows to illustrate scour mark locations and directions.

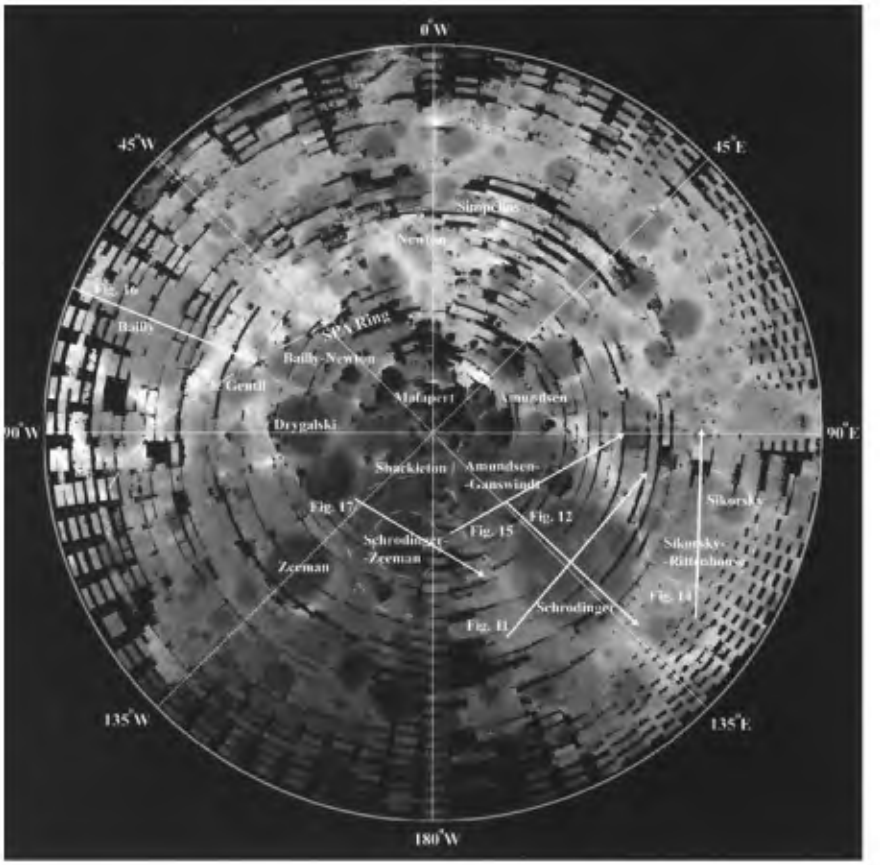


**Figure 10.** Locations of topographic profiles and selected named features in the south polar area overlain on a grey-scale DEM (black <= −8.7 km, white >= +4.8 km, and no data is also designated black). The rings of some of the more degraded basins have been indicated by dashed lines.

tered on 22°E, 52°S, diameter 700 km) farther to the north. Some of the deepest points of the SPA basin occur close to the interior of the rim near the south pole.

### 4.8. Drygalski Area

Material from the pre-Nectarian Drygalski (85°W, 79°S, ~155 km diameter) crater (Plate 2b and Figures 10 and 19) appears to have collapsed onto the floor of an unnamed older intersecting (112°W, 81°S, ~140 km diameter) crater to the west and formed a deposit at least 1.4 km thick. To the north of the Drygalski-unnamed crater boundary, lies several isolated peaks spanning +1.7 km to +4.7 km (~100°W, 73°S–78°S) in absolute elevation which may form part of an inner SPA rim or perhaps the rim of a highly degraded basin yet to be identified.

### 4.9. Bailly-Newton Basin

We have discovered, with the aid of anaglyph imagery, the remains of the southern and western outer rim of a 330 km diameter basin (centered on 57°W, 73°S), here referred to as the Bailly-Newton basin. The southern rim lies on the western edge of a triangular plateau between Drygalski (85°W, 79°S) and le Gentil (76°W, 75°S) craters. The location of the Bailly-Newton basin topography is difficult to discern in the DEM alone (Figure 20) and this is possibly because the basin contains a mixture of Imbrium, Nectarian, and pre-Nectarian materials, resulting in its topography being heavily modified. Also, intriguingly, the rim of the ancient SPA basin can be seen bisecting not only the rim but also across the floor of the Bailly-Newton basin, hence the preexisting SPA topography has apparently been preserved during the formation of the Bailly-Newton basin.

## 5. Discussion and Conclusions

Our DEMs cover regions for both poles that were previously without topographic coverage, as they lie above the latitude cutoff of the Clementine laser altimeter and on the far side

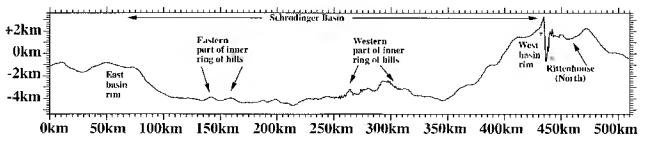


**Figure 11.** Topographic profile (E-W) through the Schrödinger basin (160°E, 73°S to 100°E, 73°S) with 10X vertical exaggeration.

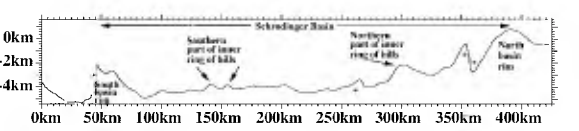


**Figure 12.** Topographic profile (S-N) through the Schrödinger basin (133°E, 82°S to 133°E, 68°S) with 10X vertical exaggeration.

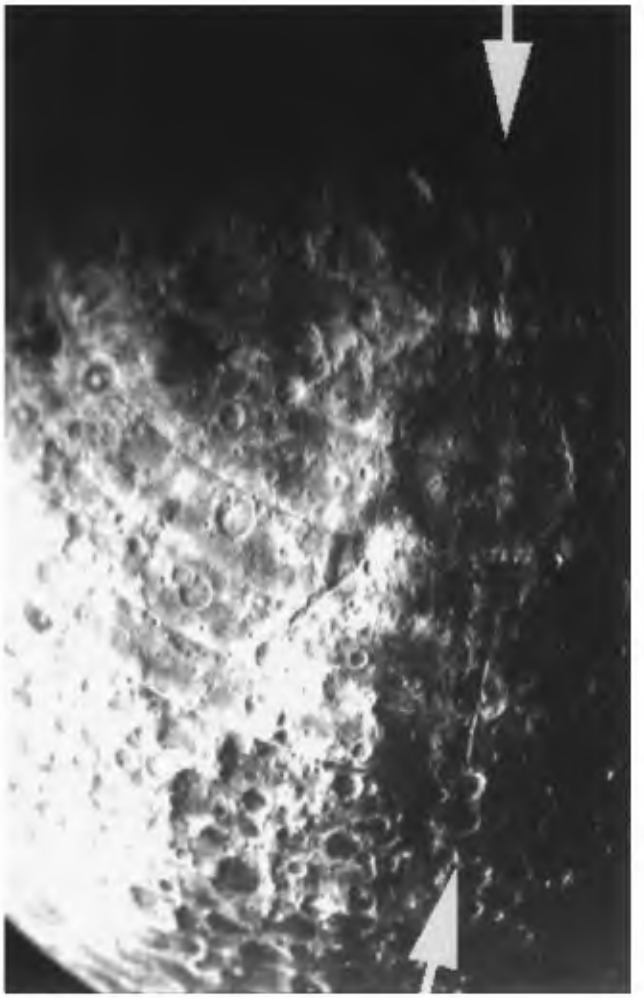

**Figure 13.** Lunar Orbiter IV 10M NASA-rectified image of the region around Schrödinger crater. Note Rima Schrödinger and the linear features between the two arrows. The banded arcs are processing artifacts.

beyond the limits of Earth-based radar. The DEMs are at a much finer spatial resolution than was obtained by the laser altimeter at lower latitudes and reveal topography that is not always apparent in spacecraft imagery due to the limitation of lighting conditions. We have been able to characterize several topographic features and discovered three previously unknown pre-Nectarian basins and verified two suspected pre-Nectarian basins. These basins and the recently confirmed Dirichlet-Jackson basin [*Cook et al.*, 1999b] increase the number of known pre-Nectarian basins [*Wilhelms*, 1987; *Spudis*, 1993; *Spudis et al.*, 1994] larger than 300 km in diameter from 32 to 36 (13% increase).

Although our results have provided new information about the relative topography in the lunar polar regions, estimates of

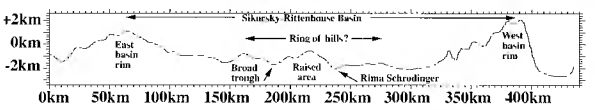


**Figure 14.** Topographic profile through the Sikorsky-Rittenhouse basin (125°E, 65°S to 89°E, 69°S) with 10X vertical exaggeration.

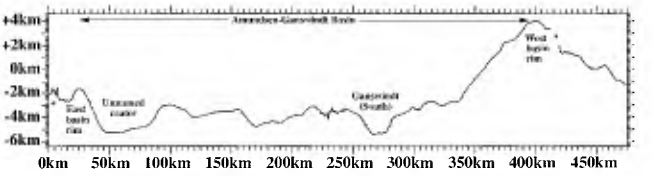


**Figure 15.** Topographic profiles through the Amundsen-Ganswindt basin (170°E, 82°S to 90°E, 75°S) with 10X vertical exaggeration.

absolute elevation discussed below suggest that knowledge of the absolute elevation at the lunar poles remains uncertain. An earlier Clementine laser altimeter interpolation study suggested that topography in the south polar region was $-1 \pm 2$ km [*Zuber and Smith*, 1997], but this was based on an interpolation over ~20° of latitude (600 km). Analysis [*Shevchenko and Chikmachev*, 1998] of a Russian lunar limb zone catalog [*Durma*, 1973] suggests positive absolute heights around the south pole. However, results of this study may be in doubt because their measurements for the elevations near Zeeman crater are too high in comparison with nearby Clementine laser altimeter values (145°–151°W, 72°S–77°S). An Earth-based radar estimate [*Margot et al.*, 1999] referenced to selected near-side Clementine altimeter measurements gives an absolute elevation approximately +1.6 km on the rim of the crater Shackleton (very near the south pole). Another estimate based on a localized stereo-derived (independent of Clementine altimeter measurements) DEM [*Wählisch et al.*, 1999] indicates a rim elevation of $+3 \pm 1$ km. The latter rim elevation is unlikely given the crater's location on the floor of the SPA. Our estimate for the rim of the crater Shackleton is approximately −2.9 km in absolute elevation and is lower than the previous estimates. Unlike the above mentioned estimates, our elevation result was produced using reference laser altimeter points from all available near- and far-side longitudes (excluding those that produced localized DTM tile offsets). Work at the U.S. Geological Survey (USGS) [*Rosiek et al.*, 1999a, b] utilized images from the Clementine first-month mapping orbits and rigorous photogrammetric analysis to refine the UV-VIS camera positions and orientations. These yielded absolute heights in the DEM close to the south pole of −3.9 km, which agree more closely with our results than with those of *Margot et al.* [1999] and *Wählisch et al.* [1999]. We have repeated the DTM tile-fitting process twice but, in each case, utilized an additional, artificial, laser altimeter point close to the pole (rim of Shackleton) using elevations of +1.6 km [*Margot et al.*, 1999] and +3 km [*Wählisch et al.*, 1999], respectively. Our results show that the +1.6 and +3 km elevations each produce significant topographic offset discontinuities on the lunar far side at 81°S, although the +1.6 km radar offset yields less topographic discontinuity on the lunar near side. We have also simulated shadows and compared them to Lunar Orbiter images. Whilst there is a strong resemblance, the presence of

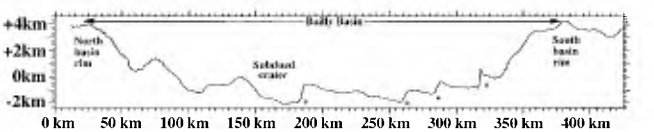


**Figure 16.** Topographic profiles through the Bailly basin (68°W, 60°S to 68°W, 74°S) with 10X vertical exaggeration.

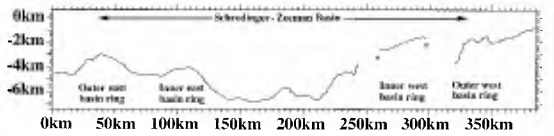


**Figure 17.** Topographic profile through the Schrödinger-Zeeman basin (130°W, 82°S to 160°E, 78°S) with 10X vertical exaggeration.

topographic noise at illumination zenith angles experienced at the poles makes interpretation difficult. However, these tests do not suggest any gross errors. Absolute height differences at the lunar north pole between radar interferometry [*Margot et al.*, 1999] derived results and our own show a closer agreement. Our results are ~1 km higher (2 km higher using the 2 km DEM pixels and second-month UV-VIS images) than the radar results.

We have found several examples where a young basin ring intersects older underlying basin rings and preserves or enhances the topography. There is one excellent example where the ring of the earlier SPA basin appears to protrude from the rim and also the floor of the Bailly-Newton basin. Intersecting basin rings may have important consequences for surface topography. In an earlier mapping of Imbrium basin topography, *Spudis* [1993] noticed that coincident rings enhanced topography, whereas noncoincidence of rings suppressed topography. In the northern Apennines the Imbrium basin rim is coincident with the main rim of the earlier Serenitatis basin; this coincidence enhances the inner basin topography, producing the Apennine Bench [*Spudis*, 1993]. However, where rings of the ancient Insularum basin [*Wilhelms*, 1987] intersect the Imbrium rim (a noncoincidence of rings), a topographic low is produced (e.g., trough west of Eratosthenes).

Results from Clementine bistatic radar experiments suggested [*Nozette et al.*, 1997] that ice is present in permanently shadowed craters close to the lunar south pole. These results have been disputed [*Simpson and Tyler*, 1999], although evidence from Lunar Prospector data supports the theory that ice is cold trapped in permanent shadows in craters near the lunar poles [*Feldman et al.*, 1998, 1999]. Analysis of lighting conditions [*Bussey et al.*, 1999] and radar topography [*Margot et al.*, 1999] suggests that there is more permanent shadow around the lunar south pole than at the north. Our stereo-derived

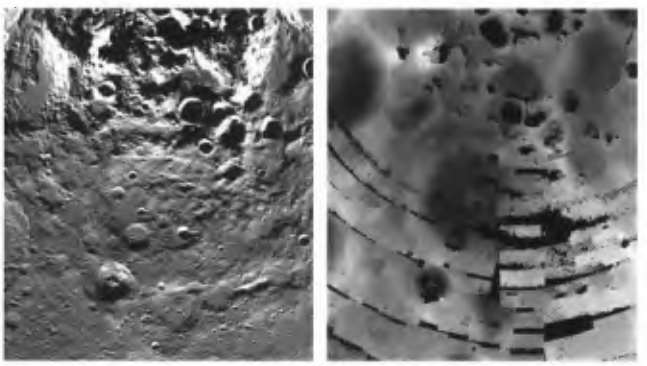


**Figure 18.** Schrödinger-Zeeman basin as depicted in (a) a Clementine UV-VIS mosaic and (b) in a grey-scale DEM (black <= −8.2 km, white >= 0.3 km, and black also represents no data).

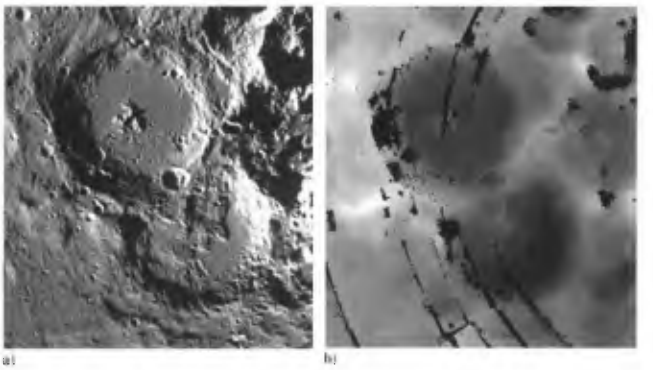

**Figure 19.** Drygalski crater showing a collapsed rim feature: (a) UV-VIS mosaic and (b) grey-scale DEM (black <= −8.5 km, white >= +3.8 km, and black also indicates no data).

DEMs cover large areas of the far side of the Moon, beyond the reach of Earth-based radar, and may assist in a more comprehensive estimate of permanently shadowed areas when questions regarding the accuracy of absolute heights and po-

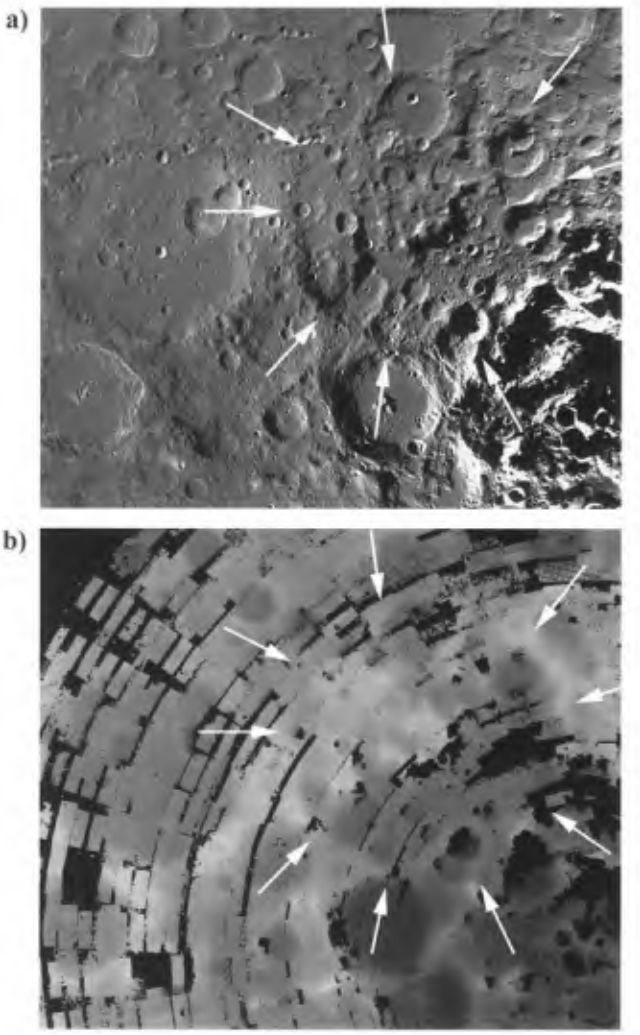


**Figure 20.** Ring of the 330 km diameter Bailly-Newton basin as indicated by arrows and seen in (a) Clementine UV-VIS mosaic and (b) grey scale DEM (black <= −9.3 km, white >= +9.9 km, and black also represents no data).

sitions at the poles are resolved. The models may also be used to estimate daytime temperatures for different depths of regolith around the poles to aid in investigating the possibility that the Prospector hydrogen signature is caused by hydrogen or ices [*Feldman et al.*, 1999] buried beneath an insulating layer of regolith.

**Acknowledgments.** We wish to thank University College London and Laser-Scan for permission to use the "Gotcha" stereomatching software, originally written by Tim Day. We would also like to thank the JPL NAIF team for providing the Clementine SPICE camera position/orientation data and DLR (German Aerospace) Berlin for 40% of the computing time for the lunar south pole DEM.

## References

Appleby, G. M., and L. W. Morrison, Analysis of lunar occultations, V, Grazing occultations 1964–1977, *Mon. Not. R. Astron. Soc.*, *205*, 57–65, 1983.

Bussey, D. B. J., P. D. Spudis, and M. S. Robinson, Illumination conditions at the lunar south pole, *Geophys. Res. Lett.*, *26*, 1187–1190, 1999.

Cook, A. C., and M. S. Robinson, The lunar South Pole from Clementine stereo imagery (abstract), paper presented at 3rd International Conference on the Exploration and Utilization of the Moon, Russ. Acad. of Sci., Moscow, 1998.

Cook, A. C., H. Hoffmann, and R. Jaumann, Digital Elevation models of lunar and martian landing sites (abstract), *Proc. Vernadsky-Brown Microsymp.*, *24*, 19–20, 1996a.

Cook, A. C., J. Oberst, T. Roatsch, R. Jaumann, and C. Acton, Clementine imagery: Selenographic coverage for cartographic and scientific use, *Planet. Space Sci.*, *44*, 1135–1148, 1996b.

Cook, A. C., P. D. Spudis, M. S. Robinson, T. R. Watters, and D. B. J. Bussey, The topography of the lunar poles from digital stereo analysis (CDROM abstract), *Proc. Lunar Planet. Sci. Conf.*, *30*, 1154, 1999a.

Cook, A. C., A. S. Konopliv, and T. R. Watters, Newly discovered lunar basins and the confirmation of suspected basins, *Proc. Vernadsky-Brown Microsymp.*, *30*, 11–12, 1999b.

Day, T., A. C. Cook, and J.-P. Muller, Automated digital topographic mapping techniques for Mars, *Int. Arch. Photogramm. Remote Sens.*, *29-B4*, 801–808, 1992.

Durma, A. C., The absolute altitudes of the marginal zone of the Moon reduced to a system of selenodetic standard elevations (in Russian), *Astrometry Astrophys.*, *20*, 55–68, 1973.

Feldman, W. C., S. Maurice, A. B. Binder, B. L. Barraclough, R. C. Elphic, and D. J. Lawrence, Fluxes of fast and epithermal neutrons from Lunar Prospector: Evidence for water ice at the lunar poles, *Science*, *281*, 1496–1500, 1998.

Feldman, W. C., S. Maurice, D. J. Lawrence, R. C. Elphic, B. L. Barraclough, and A. B. Binder, Enhanced hydrogen abundances near both lunar poles, *Lunar Planet. Inst.* [CD-ROM], abstract 8051, 1999.

Greeley, R., and R. M. Batson (Eds.), *Planetary Mapping*, 296 pp., Cambridge Univ. Press, New York, 1990.

Heiken, G. H., D. T. Vaniman, and B. M. French, *Lunar Source Book*, pp. 58–59, Cambridge Univ. Press, New York, 1991.

Hoffmann, H., A. C. Cook, C. Gritzner, J. Oberst, and B. Schreiner, LEDA remote sensing during lunar orbit operations: Requirements and mission capabilities (abstract), *Ann. Geophys.*, *14*(III), C804, 1996.

Konopliv, A. S., and D. N. Yuan, Lunar Prospector 100th degree gravity model development, (CDROM abstract), *Proc. Lunar Planet Sci. Conf.*, *30*, 1067, 1999.

Konopliv, A. S., A. B. Binder, L. L. Hood, A. B. Kucinskas, W. L. Sjogren, and J. G. Williams, The gravity field of the Moon from the Lunar Prospector mission, *Science*, *281*, 1476–1480, 1998.

Lucchitta, B. K., Geologic map of the north side of the Moon (map), *U.S. Geol. Surv.*, *Map I-1062*, 1978.

Margot, J. L., D. B. Campbell, R. F. Jurgens, and M. A. Slade, Topography of the lunar poles from radar interferometry: A survey of cold trap locations, *Science*, *284*, 58–60, 1999.

McEwen, A. S., and M. S. Robinson, Mapping the Moon by Clementine, *Adv. Space Res.*, *19*, 1523–1533, 1997.

Melosh, H. J., *Impact Cratering a Geological Process*, 245 pp., Oxford Univ. Press, London, 1989.

Nefediev, A. A., Maps of the lunar limb relief reduced into a common level (in Russian), *Proc. Engelgardt Astron. Obs.*, *30*, 1–150, 1958.

Nozette, S., et al., The Clementine mission to the Moon: Scientific overview, *Science*, *266*, 1835–1839, 1994.

Nozette, S., E. M. Shoemaker, P. D. Spudis, and C. L. Lichtenberg, The possibility of ice on the Moon, *Science*, *278*, 144–145, 1997.

Oberst, J., T. Roatsch, W. Zhang, A. C. Cook, R. Jaumann, T. Duxbury, F. Wewel, R. Uebbing, F. Scholten, and J. Albertz, Photogrammetric analysis of Clementine multi-look angle images obtained near Mare Orientale, *Planet. Space Sci.*, *44*, 1123–1133, 1996.

Rosiek, M. R., R. Kirk, and A. Howington-Kraus, Lunar topographic maps derived from Clementine imagery (CD-ROM abstract), *Proc. Lunar Planet. Sci.*, *30*, 1853, 1999a.

Rosiek, M. R., R. Kirk, and A. Howington-Kraus, Lunar south pole topography derived from Clementine imagery, New views of the Moon II: Understanding the Moon through the integration of diverse datasets, *Lunar Planet. Inst.* [CD-ROM], abstract 8046, 1999b.

Shevchenko, V. V., and V. I. Chikmachev, Model of the lunar south pole region relief (CDROM abstract), *Lunar Planet. Sci.*, *29*, 1346, 1998.

Shoemaker, E. M., M. S. Robinson, and E. M. Eliason, The south pole of the Moon as seen by Clementine, *Science*, *266*, 1851–1854, 1994.

Simpson, R. A., and G. L. Tyler, Reanalysis of Clementine bistatic radar data for the lunar south pole, *J. Geophys. Res.*, *104*, 3845–3862, 1999.

Smith, D. E., M. T. Zuber, G. A. Neumann, and F. G. Lemoine, Topography of the Moon from the Clementine lidar, *J. Geophys. Res.*, *102*, 1591–1611, 1997.

Sorensen, T. C., Global lunar mapping by the Clementine spacecraft, *Adv. Astronaut. Sci.*, *89*, 457–476, 1995.

Spudis, P. D., *The Geology of Multi-Ring Impact Basins*, 263 pp., Cambridge Univ. Press, New York, 1993.

Spudis, P. D., R. A. Reisse, and J. J. Gillis, Ancient multiring basins on the Moon revealed by Clementine laser altimetry, *Science*, *266*, 1848–1851, 1994.

Spudis, P. D., T. Cook, M. Robinson, B. Bussey, and B. Fessler, Topography of the south polar region from Clementine stereo imaging, New views of the Moon: Integrated remotely sensed, geophysical, and sample datasets, *Lunar Planet. Inst.*, [CD-ROM], abstract 6010, 1998.

Stacy, N. J. S., D. B. Campbell, and P. G. Ford, Arecibo radar mapping of the lunar poles: A search for ice deposits, *Science*, *276*, 1527–1530, 1997.

Wählisch, M., H. Hoffmann, R. Wagner, U. Wolf, A. Hoffmeister, and R. Jaumann, High resolution mosaic and digital terrain model of the lunar south pole region derived from Clementine data (CDROM abstract), *Proc. Lunar and Planet. Sci. Conf.*, *30*, 1636, 1999.

Watts, C. B., *The Marginal Zone of the Moon*, vol. 17, 951 pp., Naut. Almanac Off., U.S. Nav. Obs., Washington, D. C., 1963.

Wilhelms, D. E., The geologic history of the Moon, *U.S. Geol. Surv. Pap. 1348*, 302 pp., U.S. Govt. Print. Off., Washington, D. C., 1987.

Wilhelms, D. E., K. A. Howard, and H. G. Wilshire, Geologic map of the south side of the Moon (map), *U.S. Geol. Surv. Map*, *I-1162*, 1979.

Zuber, M. T., and D. E. Smith, Topography of the lunar south polar region: Implications for the size and location of permanently shaded regions, *Geophys. Res. Lett.*, *24*, 2183–2186, 1997.

Zuber, M. T., D. E. Smith, F. G. Lemoine, and G. A. Neumann, The shape and internal structure of the Moon from the Clementine Mission, *Science*, *266*, 1839–1843, 1994.

A. C. Cook and T. R. Watters, Center for Earth and Planetary Studies, National Air and Space Museum, Washington, D.C., 20560-0315. (tcook@ceps.nasm.edu)

M. S. Robinson, Department of Geological Sciences, Northwestern University, Evanston, IL 60208.

P. D. Spudis, Lunar and Planetary Institute, Houston, TX 77058.

D. B. J. Bussey, Space Science Department, ESA/ESTEC, Nordwijk, The Netherlands.

(Received May 12, 1999; revised November 15, 1999;
accepted December 6, 1999.)